applied sciences

MDPI

Article

Design and Experimental Analyses of an Accuracy Verification System for Airborne Target Tracking via Radar Guidance Systems

Yingchao Han [1,2], Weixiao Meng [1,*] and Xiaodong Wang [2]

[1] School of Electronics and Information Engineering, Harbin Institute of Technology, Harbin 150001, China; hanyingchao@casic.com.cn
[2] Beijing Institute of Electronic System Engineering, Beijing 100854, China; casic_wangxiaodong@126.com
* Correspondence: wxmeng@hit.edu.cn

Abstract: A radar guidance system is a core component of a radar-guided air-to-air missile, and its tracking accuracy of airborne targets determines the operational effectiveness of said missile. To verify the tracking accuracy of the radar guidance system against an airborne target under the real flight conditions of the missile, an experimental verification system was implemented in this study. The mechanical, electrical, and bus interfaces of the verification system were examined. A tracking accuracy evaluation model of the seeker was designed based on the data obtained from the experiments using the proposed test method, and the tracking accuracy of the seeker in the typical state was analyzed.

Keywords: wireless measurement analysis; seeker; radar; radio frequency data; test and experiment

Citation: Han, Y.; Meng, W.; Wang, X. Design and Experimental Analyses of an Accuracy Verification System for Airborne Target Tracking via Radar Guidance Systems. *Appl. Sci.* **2022**, *12*, 6838. https://doi.org/10.3390/app12146838

Academic Editors: Miroslav Kelemen and Saša Mladenović

Received: 4 June 2022
Accepted: 2 July 2022
Published: 6 July 2022

1. Introduction

An air-to-air missile weapon system involves a missile, which is launched either via a manned or unmanned air platform to attack valuable airborne targets. The vigorous development of new technologies, such as stealth, network, and artificial intelligence, has promoted significant changes in the field of air combat, showing stronger autonomy, abruptness, and complexity. The concept of combat has changed from absolute air control to relative air control, and then to "penetrating air traffic control" [1–4]. Since the creation of the first radar-guided air-to-air missile in the 1940s, more than ten countries and regions in the world have developed radar-guided air-to-air missiles, with more than 50 models in each development and application stage [5]. Alongside the evolution of the air combat system, the autonomous attack capability of radar-guided air-to-air missiles has become stronger and stronger, whose development has experienced four generations, marked by leapfrogging of the attack distance, attack scope, and applicable mode against different targets. The first-generation radar-guided air-to-air missile adopted the beam guidance system with fixed receiving antennas. Constrained by limited maneuverability, the carrier radar reduced the safety of the carrier aircraft while continuously illuminating the missile and target. Utilizing rear attack, these missiles can be used to attack large airborne targets with low velocity, limited maneuverability, and a low level of self-protection. The accuracy and anti-jamming ability of its radar guidance system were also poor. The second-generation radar-guided air-to-air missile was a semi-active homing guidance system, utilizing concealed conical scanning and continuous wave to attack large and medium-sized airborne targets with a certain level of maneuverability. Although it showed some improvements in operational mode when compared to first-generation missiles, the amplitude of the echo signal measured by the conical scanning mode of the radar guidance system significantly varied, and the tracking accuracy was not ideal. Hence, it failed to independently accomplish attack tasks, i.e., without the support of the carrier aircraft, which limited its capability in combat. The third-generation radar-guided air-to-air missile

adopted the monopulse semi-active homing guidance mode. When compared to second-generation missiles, its angle measurement accuracy and combat jamming countermeasure capability were significantly improved. Even though an omni-directional attack centered on the target was realized, the operation still relied on continuous illumination of the airborne radar. Additionally, with an obvious defect in the late separation of the carrier aircraft, while the missile is attacking the target, the survivability of the aircraft can be highly threatened [6–10]. The fourth-generation radar-guided air-to-air missile adopted the compound guidance system of inertial or satellite plus data link plus active radar, which offered a closed system for medium- and long-range attacks and significantly enlarged the combat distance. It is characterized by omni-directional attacks, all-weather day-and-night operations, and multi-target attacks. After adopting the anti-jamming integrated design of active radar guidance and guidance control systems, as well as multiple digital signal processing technologies, it exhibits a stronger anti-jamming capability. Meanwhile, the innovative design in the operational mode post-launch improved the survivability of the carrier aircraft. Additionally, it can receive guidance from another aircraft, which deepens the integration with the platform and combat system and realizes a substantial leap in combat operational mode [11–14].

In conclusion, a radar guidance system is a core component of a radar-guided air-to-air missile, which is responsible for the search, interception, and tracking of the target to attack. Meanwhile, it provides the missile guidance system with the necessary information to accomplish its tasks. During the evolvement of missiles, according to the design characteristics, working principle, and operational environment of the guidance system, the tracking accuracy requirements of its radar guidance system also differ. In this study, a "target situational awareness" test system was designed for the purposes of evaluating the target interception and tracking performance of the radar seeker during the post-launch flight, thereby verifying the mission reliability in terms of time sequence across the entire workflow, as well as uncovering potential problems to the maximum possible extent such as possible hardware failures and parameter mismatch of the missile in the flight environment. The bus interface, mechanical interface, electrical interface, power supply, data format, working time sequence, and other key technologies required for coordination between the carrier aircraft and pod were implemented. Furthermore, the test data analysis model was examined using the aforementioned technologies. Additionally, the feasibility of the test system was evaluated and the accuracy of airborne target tracking via a typical seeker was analyzed.

2. Composition of the "Target Situational Awareness" Test System and Experimental Methods

2.1. Objectives of the Test System

The composition of the "target situational awareness" test system is shown in Figure 1. The pod flight was mounted on the aircraft to simulate the flight state of the missile after launch, and a typical aircraft was used to simulate the target aircraft tracked by the airborne radar and pod seeker. According to the preset operating procedures and time sequence, while the pod is flying toward the target carried by the aircraft, the airborne radar intercepts and tracks the target aircraft and sends the tracking target information to the pod. Data calculation was conducted by the pod, and the autonomous flight state was simulated based on the designated time sequence as well as the attack process of target interception and tracking by the radar guidance system in the pod.

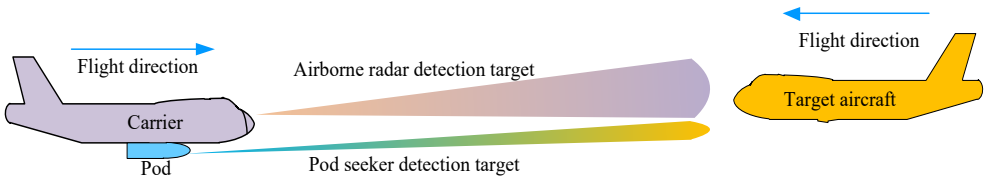

Figure 1. Composition of the "target situational awareness" test system.

The test system aimed at solving the following problems: Upon modification, the shape and structure of the pod should satisfy the flight safety requirements of the carrier in terms of structure and strength; the control of multiple transitions from hanging flight state to simulated attack state should be involved in the tests; power supply and long-time cooling of high-power equipment on the missile should be involved in the transition of multiple attack states; data recording of the carrier, missile, and target aircraft should be conducted during tests; and operational control of the time sequence and work mode of the carrier, missile, target aircraft, and other test equipment should be performed [10,15–19].

2.2. Carrier Aircraft and Pod Being Tested

2.2.1. Safe Hanging Design of The Pod Being Tested

To ensure stable and reliable hanging of the pod under various maneuvering flight conditions, the mechanical interface between the pod and carrier was devised as "TUTU four sliders". The "T"- and "U"-shaped structures are shown in Figure 2.

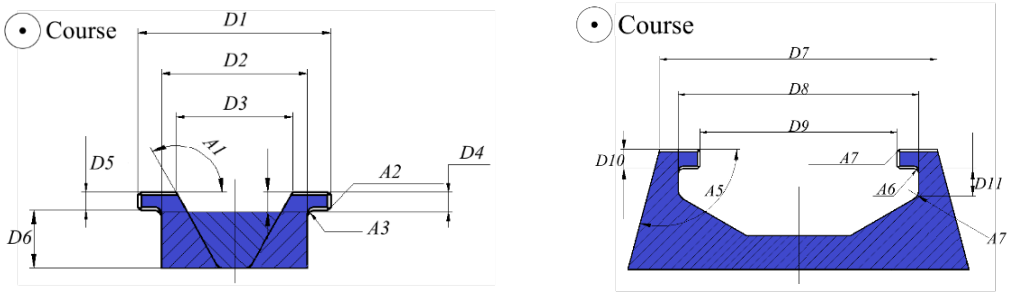

(**a**) (**b**)

Figure 2. Structural diagram of the hanging mechanism. (**a**) "T"-shaped structure, (**b**) "U"-shaped structure.

In the "T"-shaped structure, parameters D1–D6 are the length control variables, and A1–A3 correspond to the angle control variables. In the "U"-shaped structure, parameters D7–D11 correspond to the length control variables, and A5–A7 correspond to the angle control variables.

TMUI 250 maraging steel ($\sigma_m \geq 1760$ MPa) was selected as the material for the "T"- and "U"-shaped structures, and the structures were fabricated via wire cutting. As shown in Figure 3, the results of the finite element analysis suggest that the maximum axial and normal stresses of the cabin body at the connection between the hanging mechanism and pod body correspond to 349.17 MPa and 285.73 MPa, respectively. These results indicate that this structure can effectively withstand the stress load during the hanging flight.

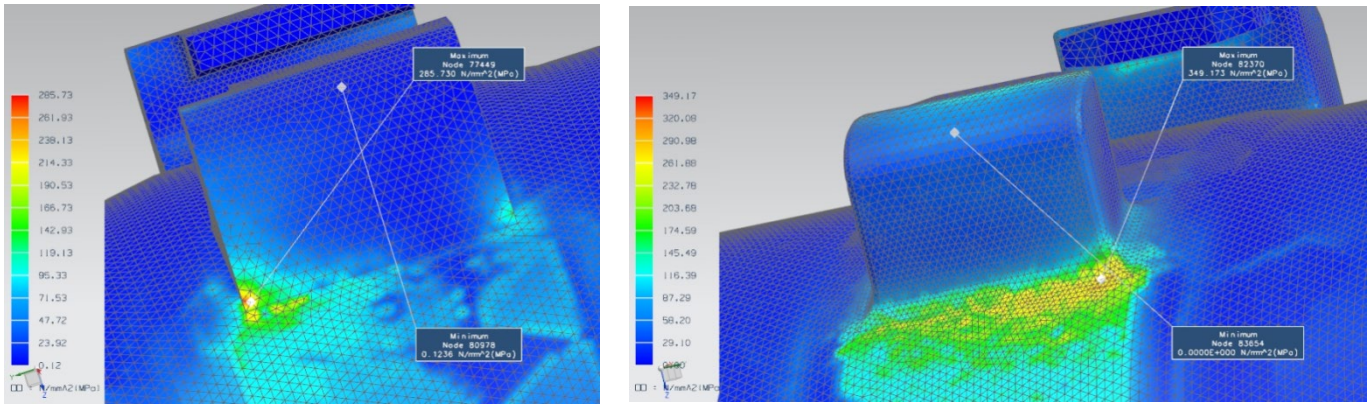

Figure 3. Simulation analysis of the vibration stress distribution.

To further verify the strength of the hanging mechanism, a functional vibration test of the pod was conducted using the vibration platform, and the vibration spectrum is shown in Figure 4.

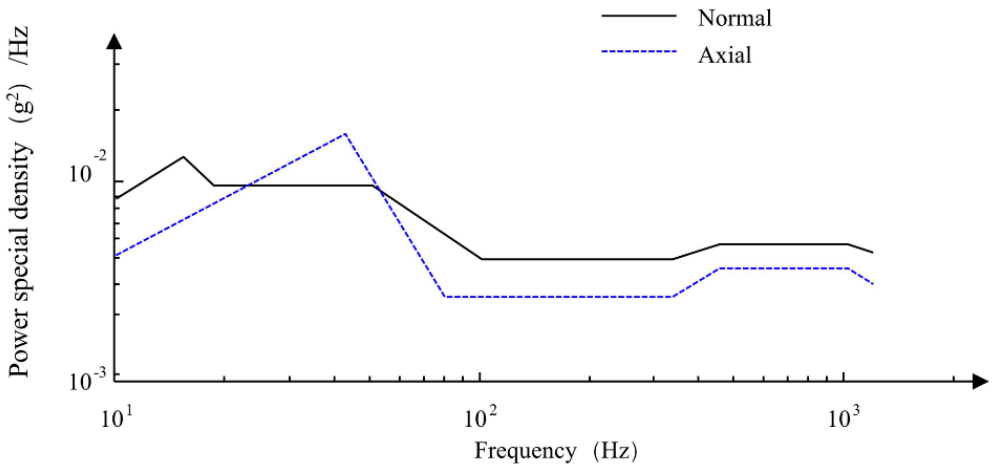

Figure 4. Vibration spectrum.

After the vibration test, the structure was sampled transversely and longitudinally. The metallographic morphology images are presented in Figure 5 at a magnification of 200. Typical morphology of cracks, such as stripes, was not observed. Hence, it was assumed that the structure can effectively cope with the stress load during hanging flight.

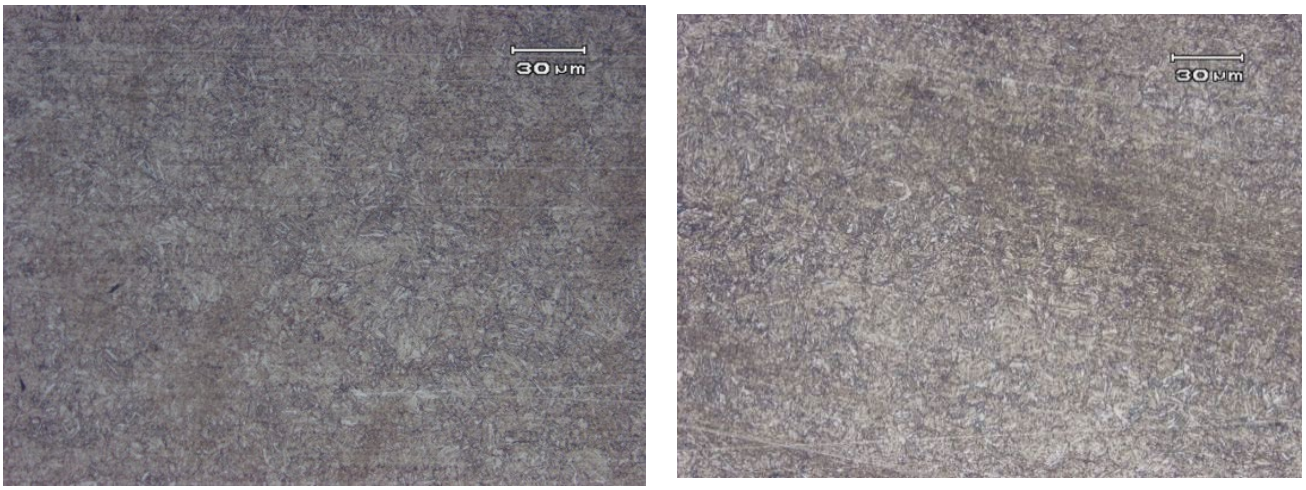

Figure 5. Metallographic morphology of the transverse and longitudinal structure of the "T"-shaped structure.

2.2.2. Design of the Communication Bus Interface

In the experiments, the carrier flight interacted with the pod via buses to accomplish data transmission, as well as to send and receive control instructions referring to the downlink data sent by the carrier and uplink data sent by the missile. The data sent by the carrier to the pod via the 1553B bus included the following categories:

① Description of the carrier aircraft, including necessary carrier information, ID number, and code, which were sent to the pod. As shown in Table 1.

② Instructions of the carrier, which were sent to the pod, including simulated launch and pod preparation. As shown in Table 2.

③ Mission parameters, including parameters of the carrier aircraft to be sent to the pod, such as carrying time, velocity X, velocity Y, velocity Z, pitch angle, heading angle,

rolling angle, wind velocity X, wind velocity Y, wind velocity Z, latitude, longitude, and altitude. As shown in Table 3.

Table 1. Description of the carrier.

No.	Item	Unit	Bit	Accuracy	Note
1	ID number	-	16	-	ASCII code
2	Identification	-	32	-	ASCII code
3	Pod hanging condition	-	8	-	1: Hanging pod; 0: No pod

Table 2. Instructions of the carrier.

No.	Item	Unit	Bit	Accuracy	Note
1	Simulated launch of the pod	-	1	-	1: Launch; 0: Not launched
2	Pod preparation	-	1	-	1: Prepare; 0: Not prepared

Table 3. Mission parameters.

No.	Item	Unit	Bit	Accuracy	Note
1	Carrier time 1		16	-	Year, month, day
2	Carrier time 2	us	32	-	Hour, minute, second
3	Data frame counter		16	1	For every frame of data sent to the pod, the counter increases by 1
4	Carrier velocity X	m/s	16	0.025	
5	Carrier velocity Y	m/s	16	0.025	-
6	Carrier velocity Z	m/s	16	0.025	
7	Carrier pitch angle	m/s	16	0.0055	
8	Carrier heading angle	m/s	16	0.0055	-
9	Carrier roll angle	m/s	16	0.0055	
10	Wind velocity X	m/s	16	0.025	Northward wind velocity
11	Wind velocity Y	m/s	16	0.025	Westward wind velocity
12	Wind velocity Z	m/s	16	0.025	Skyward wind velocity
13	Mach number	Ma	16	0.0001	Mach number of the carrier flight
14	Carrier latitude	°	32	8.381903×10^{-8}	0: North latitude; 1: South latitude
15	Carrier longitude	°	32	8.381903×10^{-8}	0: East longitude; 1: West longitude
16	Carrier altitude	m	16	1.28	-

④ Target parameters, including generation time of the target information, its longitude, latitude, height, velocity X, velocity Y, and velocity Z. As shown in Table 4.

Table 4. Target parameters.

No.	Item	Unit	Bits	Accuracy	Note
1	Target information generation time 1		16	-	Year, month, day of the generation time
2	Target information generation time 2	us	32	40	Hour, minute, second of the generation time
3	Target latitude	°	32	8.381903×10^{-8}	0 in the sign bit signifies the north latitude; 1 the south latitude.
4	Target longitude	°	32	8.381903×10^{-8}	0 in the sign bit signifies the east longitude; 1 the west longitude.
5	Target altitude	m	16	1.28	-
6	Target velocity X	m/s	16	0.0512	-
7	Target velocity Y	m/s	16	0.0512	
8	Target velocity Z	m/s	16	0.0512	

Information Transmitted by the Pod

① Description of the pod, which was one-time valid information, including type, model number, and ID. As shown in Table 5.

Table 5. Description of the pod.

No.	Item	Unit	Bit	Accuracy	Note
1	Country code	-	16	-	ASCII code
2	Type	-	2	-	ASCII code
3	Model number	-	3	-	ASCII code
4	Code of the design organization	-	5	-	ASCII code
5	ID of the hanging object	-	48	-	ASCII code

② Pod responses, which were sent to the carrier aircraft to respond to its general instructions, including pod preparation status, simulated launch status, and self-check status. As shown in Table 6.

Table 6. Responses of the pod.

No.	Item	Unit	Bit	Accuracy	Note
1	Simulated launch status	-	1	-	1: To launch; 0: Not to launch
2	Preparation status	-	1	-	1: To prepare; 0: Not to prepare
3	Pod status	-	2	-	11: Normal; 10: Malfunction; 00: Invalid
4	Preparation results	-	2	-	11: Ready; 10: Not ready; 01: In preparation; 00: Invalid
5	Self-check results	-	1	-	1: Self-check finished; 0: Self-check unfinished

2.2.3. Design of the Power Supply and Electrical Control Interface

The required power supply to the carrier in the test system included a 45 V DC source "DC A" and a 150 V AC source "AC B". "DC A" was used for maintaining the major power supply for the continuous operation of the pod equipment (with the exception of the radar seeker), and the power supply can be switched on and off according to the control instruction during the pod-hanging flight. "AC B" supplied the refrigeration equipment in the pod, as well as the high-voltage power supply to enable multiple turning-on operations of the pod radar seeker. The operation timing of both "DC A" and "AC B" were controlled by the test sequence, as shown in Figure 6.

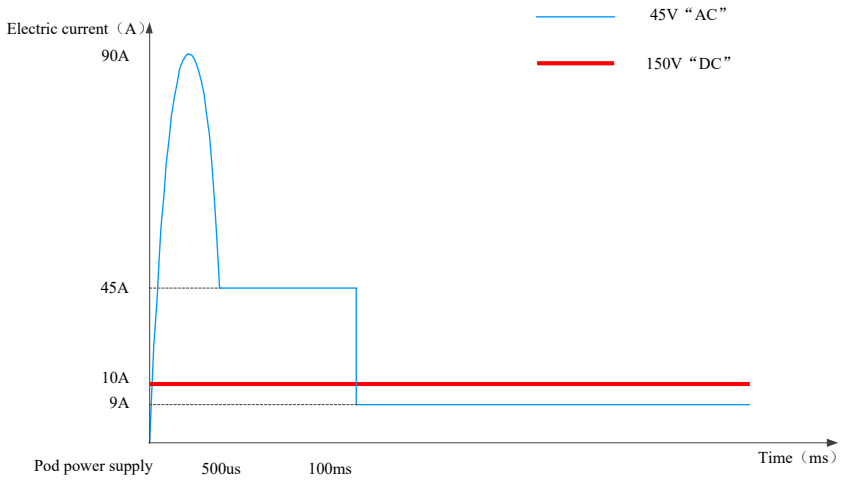

Figure 6. Power supply timing sequence.

The electrical interface between the carrier and pod was realized via a cable connection, as shown in Table 7, which mainly included (1) the "in-place status" and "in-place loop", forming a closed-loop circuit with the carrier to complete the inspections on whether the

pod is in place and whether the electrical connection is checked and confirmed; (2) the "DC A" and "DC A loop" were in charge of the DC power supply to the pod; (3) "multiplex bus A" and "multiplex bus B" were in charge of sending and receiving data between the carrier and pod; (4) "AC B1", "AC B2", and "AC B3" provided the AC power supply to the pod; (5) "structural grounding" was realized via the grounding wire; (6) the "satellite signal" transmitted the satellite signal from the carrier to the pod; (7) the telemetry and forwarding signal transmitted the telemetry signal from the pod to the carrier, which was then recorded and stored by the carrier.

Table 7. Design of the electrical interface.

No.	Electrical Interface	Signal Format
1	In-place status	-
2	Interlock loop	-
3	DC A	45 V
4	DC A loop	-
5	Multiplex bus A	1553B
6	Multiplex bus B	1553B
7	AC B1	150 V
8	AC B2	150 V
9	AC B3	150 V
10	AC neutral wire	-
11	Structural grounding	Connected to the shell of the carrier body
12	Satellite signal	GPS
13	Telemetry forwarding signal	-

2.2.4. Design of the Pod

The proposed block diagram of the pod is shown in Figure 7, which is composed of a radome, a seeker, a network of cables, an electrical connector and a connecting cable, a cabin, a control device, an inertial measuring device, water-cooling equipment, a storage battery, a GPS station and its antenna, a telemetry antenna, and a data recorder. The radome was locked by radial screws via the joints between the cabins, and the radome was located at the head of the pod, which was subject to pneumatic heating and overload during the test to ensure the normal operation of the seeker. The seeker was placed in the radome to intercept and track the target aircraft selected by the test system, as well as to provide the target information to the control device. The control device conducted calculations for the pod and issued control instructions to each piece of equipment according to the defined time sequence in the test and responded to the carrier's instructions. The storage battery provided the required power supply for the pod, the water cooling equipment offered a cooling path for the seeker to operate for a long time, and the data recorder oversaw data recording on the pod for analysis after the test.

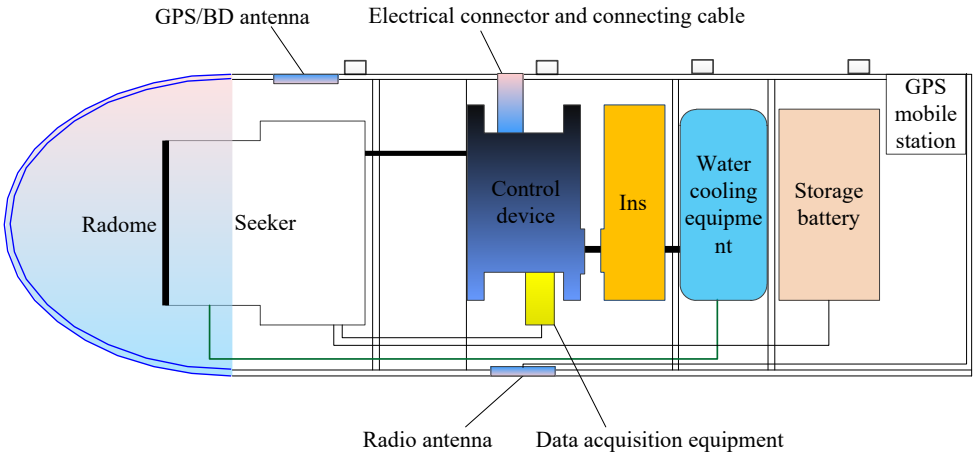

Figure 7. Composition of the pod.

2.3. Design of the Time Sequence in the Tests

An individual time sequence of the designed workflow is shown in Figure 8.

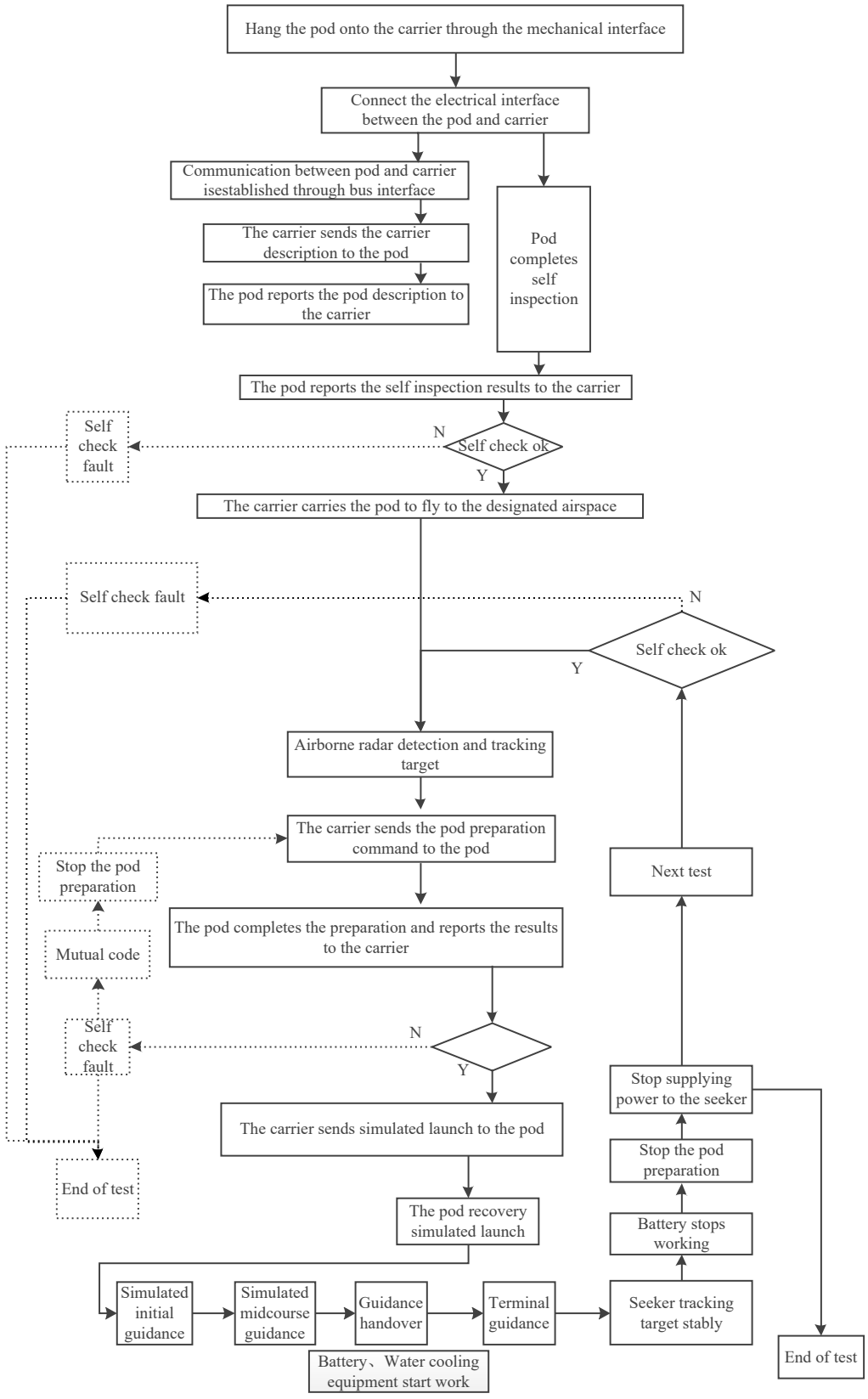

Figure 8. Time sequence of the workflow.

3. Data Analyses

3.1. Data Groups and Acquisition

The data obtained by the test system included carrier bus data, carrier GPS/BD reference data, target GPS/BD reference data, airborne radar measurement data, and pod measurement data.

Among the aforementioned data, the carrier bus data included data generation time t_{air}, carrier inertial navigation output position longitude L_{air_INS} (rad), latitude B_{air_INS} (rad), and height H_{air_INS} (m). The carrier aircraft GPS/BD reference data included carrier GPS/BD time scale T_{air} (s), carrier longitude L_{air} (rad), latitude B_{air} (rad), height H_{air} (m), and carrier velocity V_{air} (m). The target GPS/BD reference data included target GPS/BD time stamp T_{aim} (s), target longitude L_{aim} (rad), latitude B_{aim} (rad), and height H_{aim} (m). The airborne radar measurement data included target longitude L_{aim_radar} (rad), latitude B_{aim_radar} (rad), height H_{aim_radar} (m), and velocity V_{aim_radar} (m). The pod measurement data included the target measurement information output by the seeker [20–23].

3.2. Design of the Evaluation Model

Utilizing L_{air}, B_{air}, and H_{air} in the GPS/BD data of the carrier, cartesian coordinates X_{air_CGCS}, Y_{air_CGCS}, and Z_{air_CGCS} of the carrier in the CGCS2000 coordinate system were obtained via coordinate transformation.

Similarly, from L_{aim}, B_{aim}, and H_{aim} in the GPS/BD data of the target aircraft, the cartesian coordinates X_{aim_CGCS}, Y_{aim_CGCS}, and Z_{aim_CGCS} of the target position in the CGCS2000 coordinate system were obtained.

Next, the position of the target in the launch coordinate system at moment t_F, when the "simulated launch" instruction was issued by the carrier to the pod, was calculated. The launch coordinate system was defined with the launch point being origin O_F. Furthermore, the OX_F axis was in the horizontal plane crossing the origin and pointing to the north direction; meanwhile, the OY_F axis was in the vertical plane of the OX_F axis, perpendicular to the OX_F axis, and the upward direction was assigned as positive. Additionally, the OZ_F axis complied with the right-hand rule to form the coordinate system with the two axes defined above.

Using the longitude L_{aim_radar}, latitude B_{aim_radar}, and altitude H_{aim_radar} of the target aircraft measured by the airborne radar, the cartesian coordinates $X_{aim\_radar\_CGCS}$, $Y_{aim\_radar\_CGCS}$, and $Z_{aim\_radar\_CGCS}$ of the target in the CGCS2000 system were obtained by coordinate transformation.

By using the output longitude L_{air_INS}, latitude B_{air_INS}, and altitude H_{air_INS} of the main inertial navigation system of the carrier, its cartesian coordinates $X_{air\_INS\_CSCS}$, $Y_{air\_INS\_CSCS}$, and $Z_{air\_INS\_CSCS}$ in the CGCS2000 system were obtained by coordinate transformation. Then, the position measurement of the target aircraft in the launch coordinate system of the carrier could be calculated as follows:

$$\begin{bmatrix} X_{aim\_radarF} \\ Y_{aim\_radarF} \\ Z_{aim\_radarF} \end{bmatrix} = \begin{bmatrix} -cosL_{air}sinB_{air} & -sinL_{air}sinB_{air} & cosB_{air} \\ cosL_{air}cosB_{air} & sinL_{air}cosB_{air} & sinB_{air} \\ -sinL_{air} & cosL_{air} & 0 \end{bmatrix} \cdot \begin{bmatrix} X_{aim\_radar\_CGCS} - X_{air\_INS\_CSCS} \\ Y_{aim\_radar\_CGCS} - Y_{air\_INS\_CSCS} \\ Z_{aim\_radar\_CGCS} - Z_{air\_INS\_CSCS} \end{bmatrix} \quad (1)$$

The position error of the target aircraft measured by the airborne radar was then obtained.

$$\begin{bmatrix} \Delta X \\ \Delta Y \\ \Delta Z \end{bmatrix} = \begin{bmatrix} X_{airF} \\ Y_{airF} \\ Z_{airF} \end{bmatrix} - \begin{bmatrix} X_{aim\_radarF} \\ Y_{aim\_radarF} \\ Z_{aim\_radarF} \end{bmatrix} \quad (2)$$

Next, the spatial pitch angle φ_{YG} and course angle φ_{ZG} of the line-of-sight vector between the carrier aircraft and target in the carrier's launch coordinate system could be

calculated utilizing the measurement data from the airborne radar. Consequently, the angle measurement error of the airborne radar could be acquired as follows:

$$\begin{aligned} \Delta\varphi_{YRAD} &= \varphi_{YG} - \varphi_{YR} \\ &= arctan\left(\frac{Z_{aim\_radarF}}{X_{aim\_radarF}}\right) - arctan\left(\frac{Z_{aimF}}{X_{aimF}}\right) \end{aligned} \tag{3}$$

$$\begin{aligned} \Delta\varphi_{ZRAD} &= \varphi_{ZG} - \varphi_{ZR} \\ &= arctan\left(\frac{Y_{aimF}}{(X^2_{aimF}+Y^2_{aimF}+Z^2_{aimF})^{\frac{1}{2}}}\right) - arcsin\left(\frac{Y_{aim\_radarF}}{(X^2_{aim\_radarF}+Y^2_{aim\_radarF}+Z^2_{aim\_radarF})^{\frac{1}{2}}}\right) \end{aligned} \tag{4}$$

Finally, the position and angle information of the target measured by the pod was compared to that measured by the airborne radar, and the accuracy of the measurement from the seeker to the target was obtained.

3.3. Experiments and Analyses

The simulation experiments were conducted with the implemented test system, and the obtained data were analyzed. As shown in Figure 9, the test system accomplished three autonomous flight simulations of target tracking and interception with the pod. According to the designed workflow, the carrier sent the instructions "pod preparation", "simulated launch", and "not ready" one by one to the pod. The pod responded "self-inspection ok" to the carrier's instruction "pod preparation", as well as the instructions "simulated launch" and "cancel the simulated launch". Hence, the execution process was followed appropriately. To facilitate data analysis, the interactive instructions and responses between the carrier aircraft and pod were considered as reference. The absolute numbers of the carrier's instructions were adjusted for the convenience of visualization.

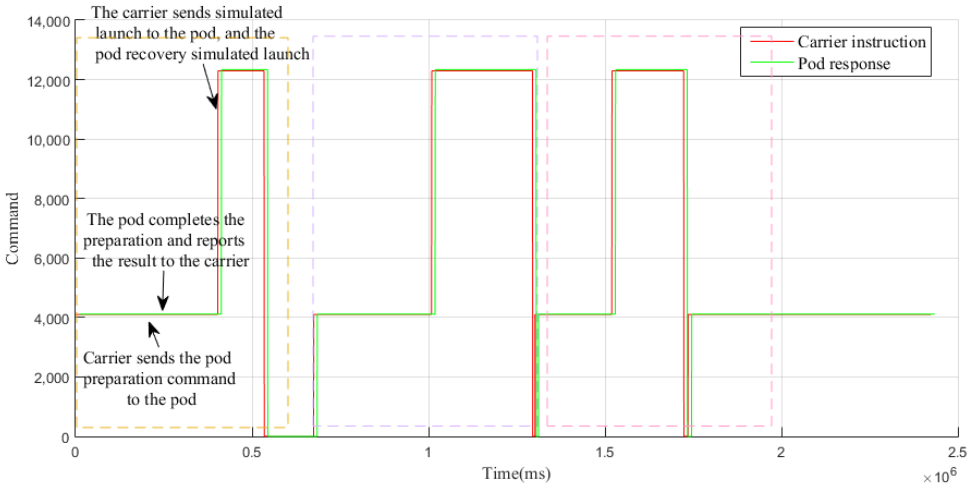

Figure 9. Timing and responses of the test instructions.

After issuing the "preparation" command, the carrier aircraft sent the initial information to the pod, including the longitude, latitude, altitude, carrier velocity X, carrier velocity Y, carrier velocity Z, pitch angle, heading angle, and roll angle, which were utilized by the pod to establish a navigation coordinate system to realize a simulated autonomous flight upon receiving the "simulated launch" command. To ensure the navigation accuracy of the pod during the handover from the midcourse to terminal guidance, the influence of wing deformation and installation error should be considered in the attitude data of the aircraft. The angle information issued by the carrier aircraft is shown in Figure 10, in which the data of the first simulated autonomous flight are enlarged and presented in Figure 11. As shown in Figure 11, the pitch and roll angles of the carrier aircraft changed continuously during the preparation phase, and continuous "S"-shaped maneuvers were

performed. The velocity information issued by the carrier to the pod is shown in Figure 12. During the demonstrated continuous "S"-shaped maneuvers, the northward and westward velocity were considered as changing accordingly, while the skyward velocity did not exhibit obvious fluctuations, which is consistent with the actual characteristics of the flight mechanics of the carrier.

When the distance between the target and carrier was 14.95 km, the carrier sent information, such as the distance, with respect to the target intercepted by the airborne radar to the pod. As illustrated in Figure 13, When the pod was 6.5 km away from the target, the battery provided a high-voltage power supply according to the predefined time sequence and transmitted the battery activation signal. As illustrated in Figure 14, when the distances between the carrier and target aircraft were between 0.53 and 0.64 km, the target aircraft turned its flight direction and accelerated to deviate from the carrier.

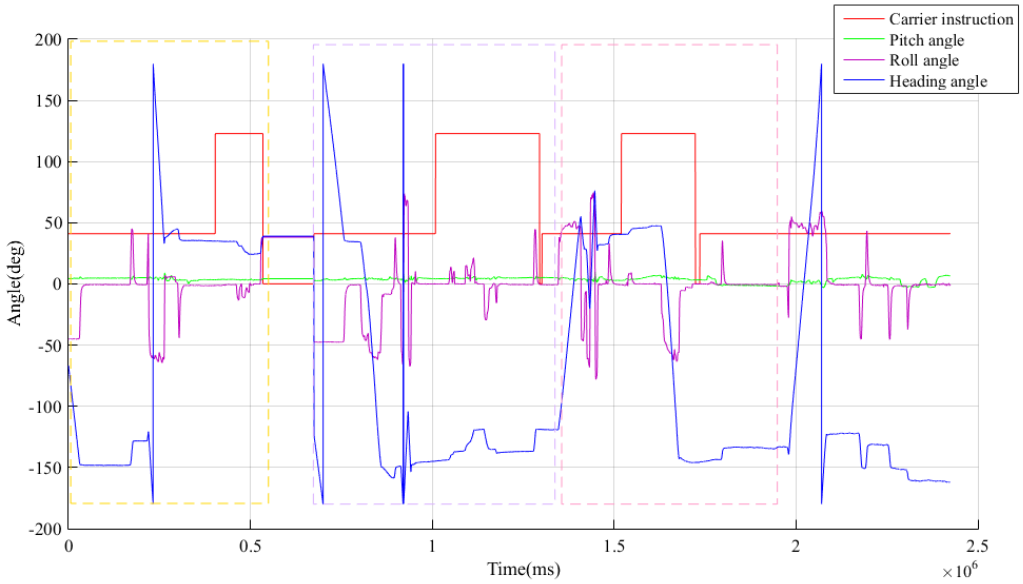

Figure 10. Angle information issued by the carrier to the pod.

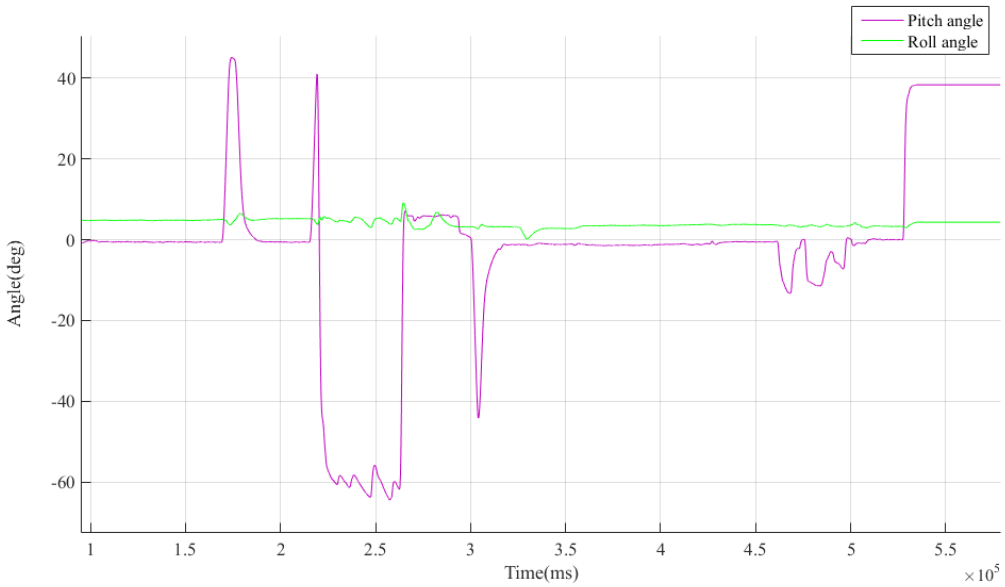

Figure 11. Angles issued by the carrier to the pod during the first simulated autonomous flight.

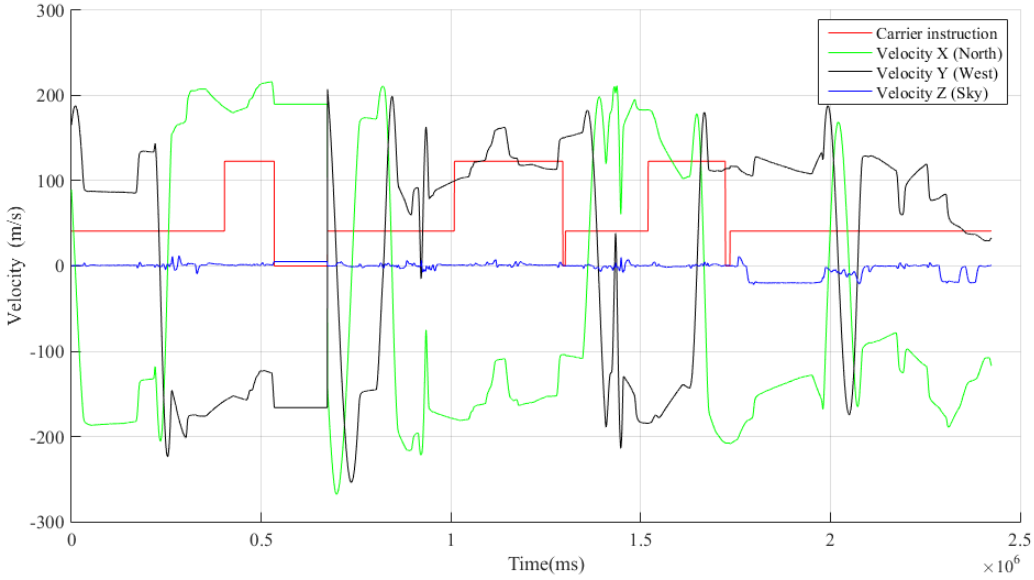

Figure 12. Speed information issued by the carrier to the pod.

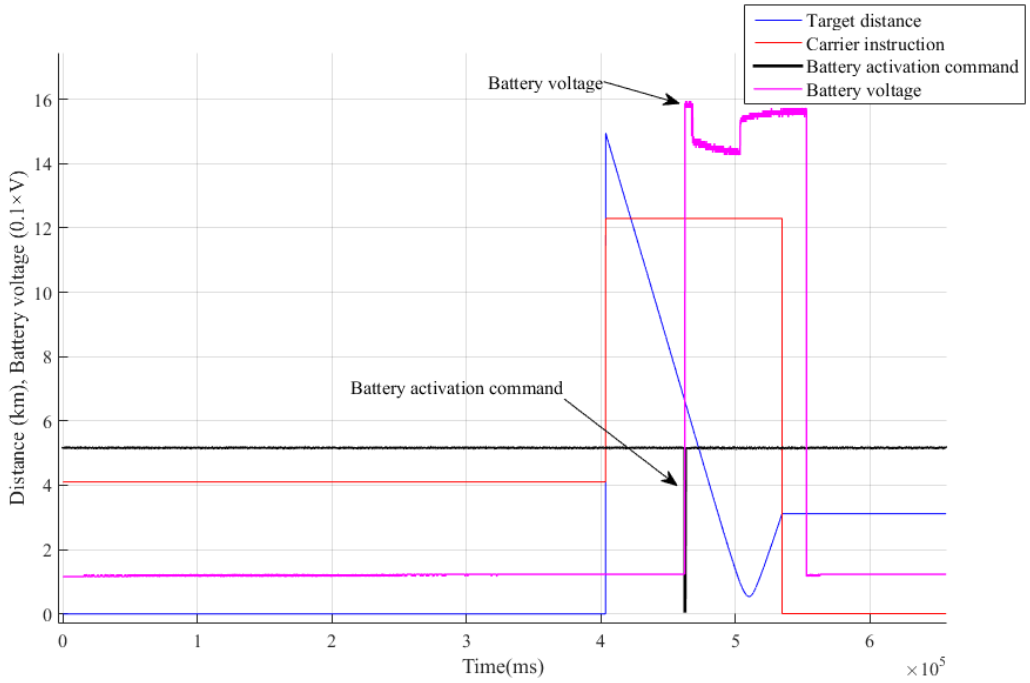

Figure 13. The pod's power supply voltage.

The launch coordinate system was established based on the evaluation model presented in Section 3.2, whose origin was defined by the location of the pod at the moment when the carrier aircraft issued the "simulated launch" instruction. The actual and measured values of the relative location between the carrier and target aircrafts were obtained from Equations (1) and (2), respectively. Consequently, the distance error of the radar tracking and measuring the target in the launch coordinate system is shown in Figure 15. When the target was approaching the airborne radar, starting from 14.95 km inward, the distance measurement error was observed as persistent. After the radar began to measure the target, the distance error converged rapidly, and the average compound spatial distance error was approximately 160 m. During the "S"-shaped maneuvers, the carrier aircraft produced more obvious fluctuations of the compound spatial distance error of approximately 50 m. With the proximity of the distance between the carrier and target, the distance error

decreased gradually, and the line-of-sight angle between the carrier and target increased gradually until the airborne radar lost the target after producing a large distance error. Based on the evaluation model introduced in Section 3.2, the compound spatial distance error was generated by the north, west, and sky distance error components. Considering the first simulated autonomous flight as an example, the three directional distance error components are shown in Figure 16.

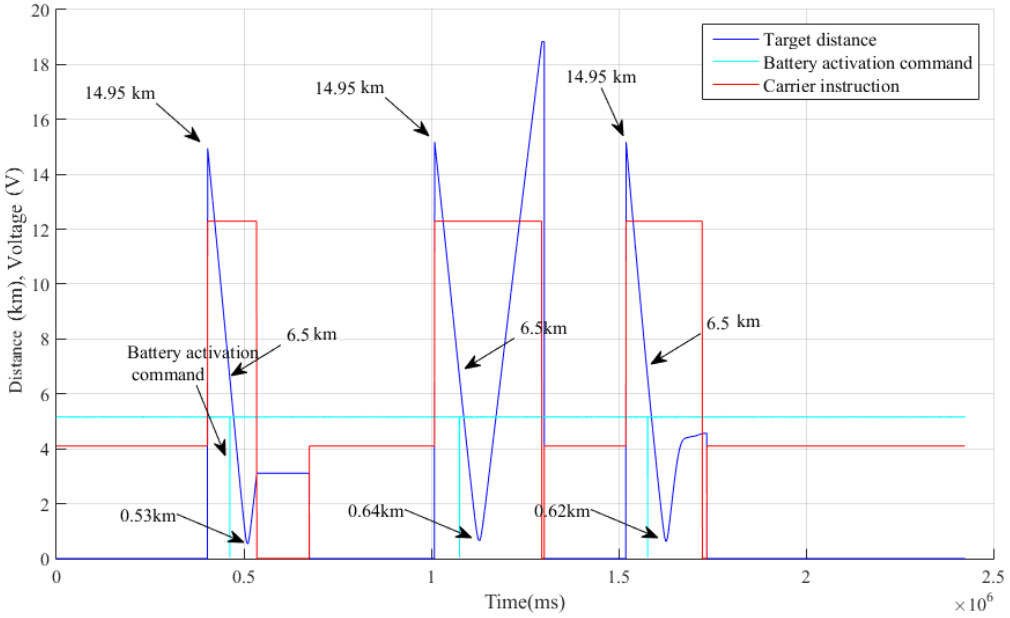

Figure 14. Time sequence of the pod's power supply.

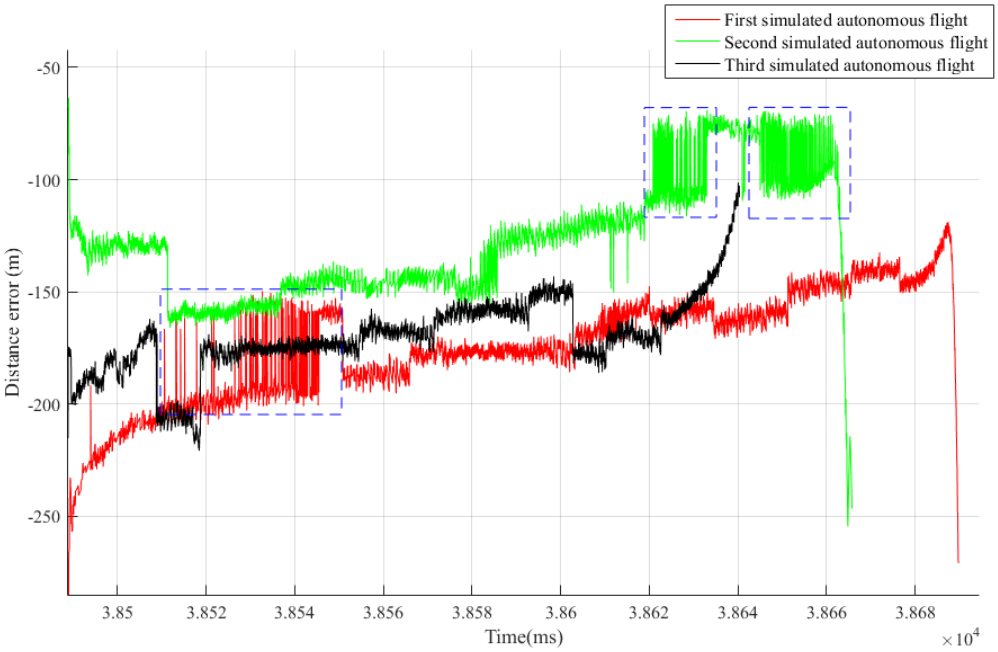

Figure 15. Spatial compound distance error of the target position measured by the airborne radar.

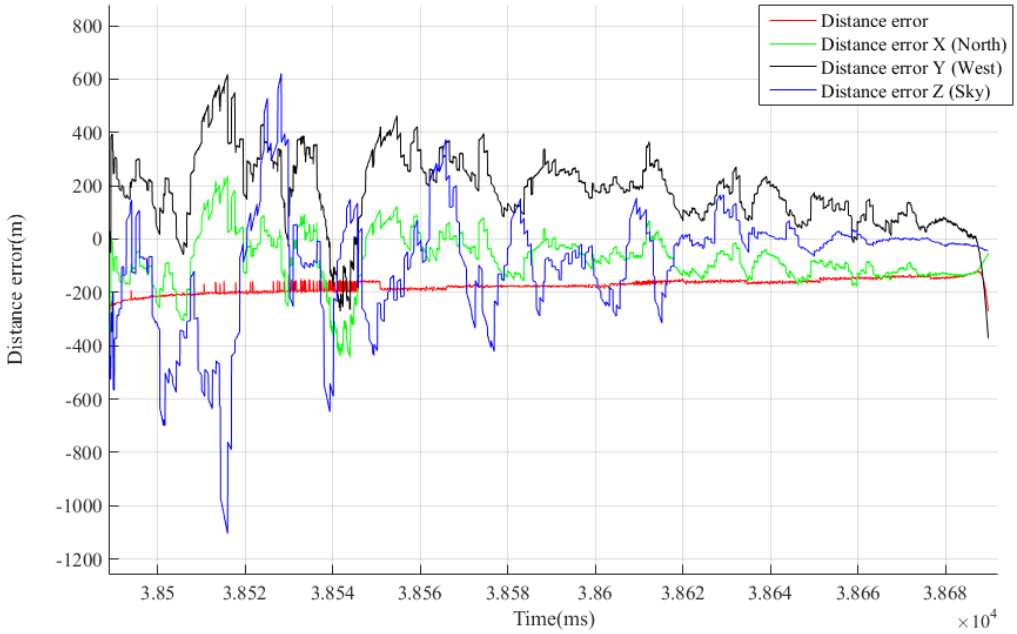

Figure 16. Distance error and its three directional components of the first simulated flight.

Furthermore, the pitch and heading angle measurement errors incurred by the airborne radar measuring and tracking the target aircraft were obtained from Equations (3) and (4), as shown in Figures 17 and 18. It can be concluded that in the stage of stable tracking of the target (excluding the target loss due to the large line-of-sight angle before the two-machine rendezvous), the average pitch and heading angle errors were 0.26° and 0.24°, respectively, and the change was considered limited when the distance varied.

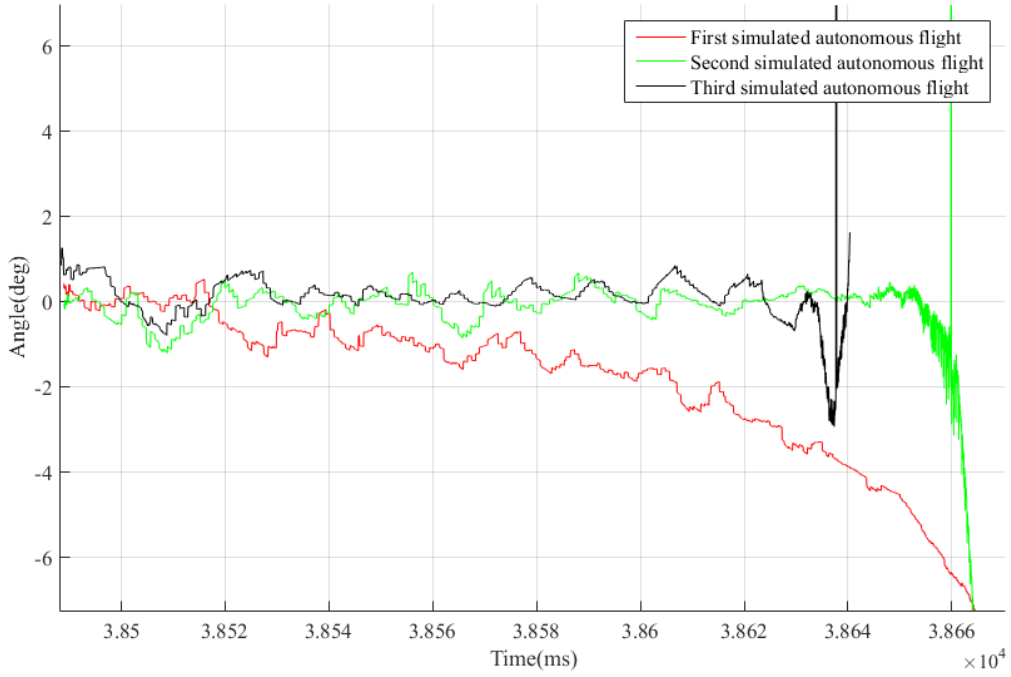

Figure 17. Pitch angle error of the target measured by the airborne radar.

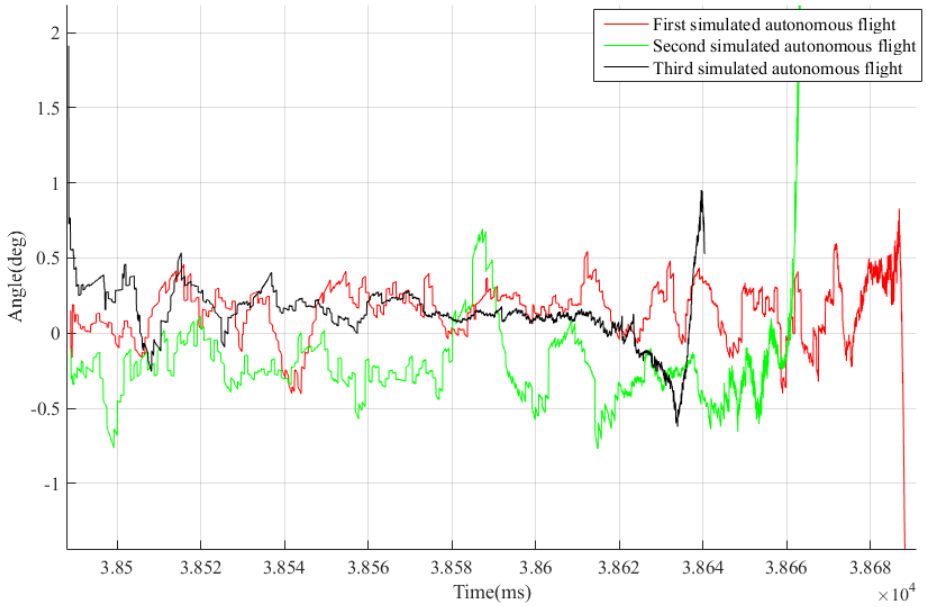

Figure 18. Heading angle error of the target measured by the airborne radar.

After receiving the target information from the carrier containing the measurement error of the airborne radar, based on the transformation and calculation, the guidance angle was generated to guide the seeker via tracking and interception of the target. The errors considered in the guidance angle included measurement errors of the airborne radar, errors in the navigation calculation of the pod (including hanging errors with the carrier such as mounting error, and transmission errors such as wing deformation), as well as errors due to the radar guidance system in the pod.

To evaluate the self-error of the guidance system, the difference between the guidance angle (recorded by the data recording device in the pod) and the intercepted target angle returned by the pod radar guidance system (recorded by the data recording device in the pod) was acquired. Considering the first simulated autonomous flight as an example, the accumulated errors of the radar guidance system intercepting the target are shown in Figure 19.

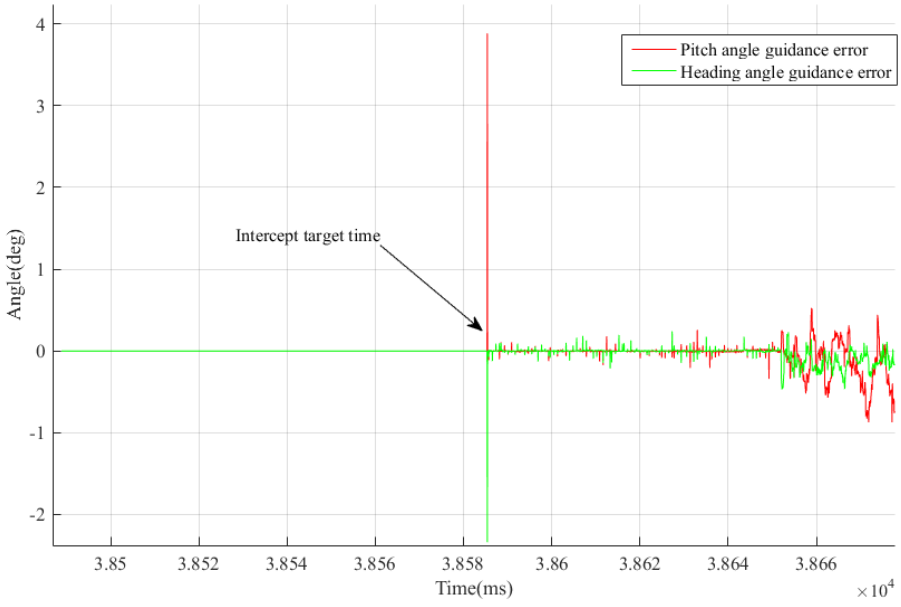

Figure 19. Accumulated errors of target interception by the radar guidance system.

Based on the difference between the accumulated errors of the target interception by the radar guidance system and target measurement errors due to the airborne radar, the error incurred by the radar guidance system was then evaluated. Subsequently, accuracy analyses of the radar guidance system under simulated flight conditions were completed. By considering the first simulated autonomous flight as an example, the intrinsic errors of the radar guidance system are shown in Figure 20.

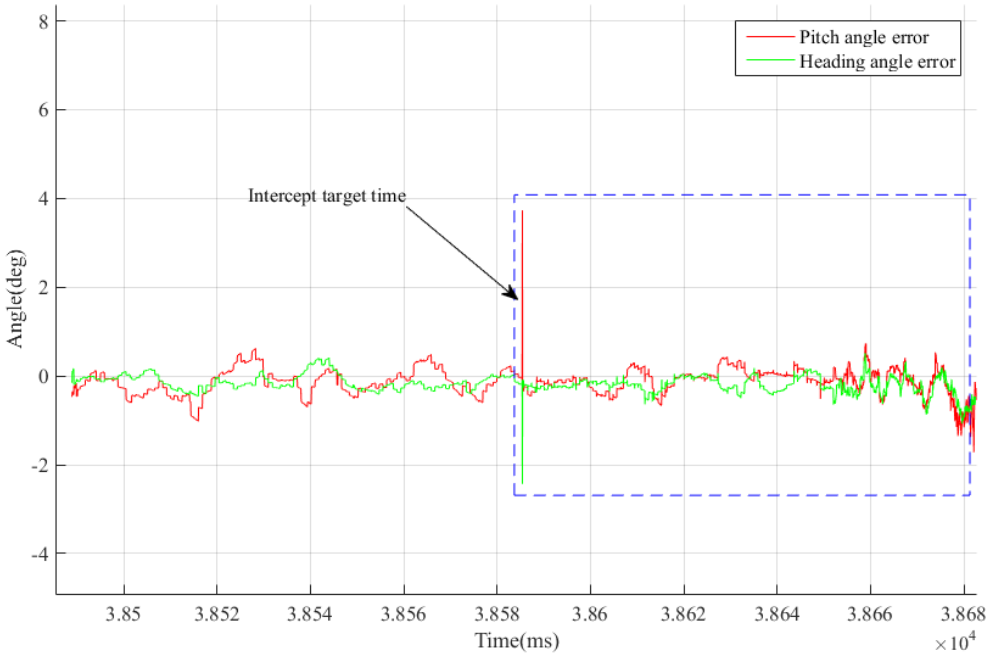

Figure 20. Intrinsic errors of the radar guidance system.

The abovementioned radar guidance system errors will adversely affect guidance accuracy. A variety of factors can cause errors, such as antenna pre-set error, electric axis null position error, antenna front installation error, thermal noise, and line of sight error of the radome. Different design schemes and production levels of radar guidance systems also lead to different levels of error influence. Antenna pre-set errors are mainly influenced by variables such as position feedback accuracy, pre-set voltage accuracy, and maximum pre-set angle. Electric axis null position error, a random constant interference, is the deviation between the null positions of the electric and mechanical axes of a radar guidance system. Seeker installation error is another random constant interference. Thermal noise can be analyzed by probability theory. Line of sight error of the radome is caused by the refraction of electromagnetic waves by the radome. It is affected by the radome's shape, material, machining precision, electric wave polarization mode, electromagnetic wave incident angle, etc. To further reduce the intrinsic errors of radar guidance systems, the abovementioned errors should be considered and strictly controlled during the design and manufacturing process.

In the above analysis, natural clutter, such as clouds and rain, was not considered. In studies that consider electromagnetic wave propagation attenuation caused by rain, clouds, and other specific working conditions and working frequency ranges of the radar, clutter should be analyzed.

4. Conclusions

In this study, we presented a tracking accuracy verification system of a radar seeker, which was composed of a carrier, target aircraft, and pod. Design schemes of the mechanical, electrical, and bus interfaces, which involved the carrier and pod, were provided. According to the defined execution flow and timing sequence of the test system, experiments and analyses were completed. Additionally, with the experimental results, a data model for

seeker accuracy analysis was designed. Moreover, a flight-tracking study of the test was conducted, and the results showed that the methodology and analysis process proposed in this study are effective.

It should be noted that this study serves more as an engineering validation. In terms of the theoretical analysis considering the causes of errors in a radar guidance system, it has limitations.

Our next step will be to examine the reasons for the errors in radar guidance systems and ways to minimize their magnitude and existence, so as to further improve the systems' detection and tracking accuracy. By developing an engineering prototype and performing flight tests, we will be able to define a clear engineering scheme that has fewer errors.

Author Contributions: Writing—original draft, Y.H.; Writing—review & editing, W.M. and X.W. All authors have read and agreed to the published version of the manuscript.

Funding: This research received no external funding.

Conflicts of Interest: The authors declare no conflict of interest.

References

1. Hughes, R. MBDA unveils future air combat weapon systems concepts. *Jane's Int. Def. Rev.* **2019**, *52*, 14.
2. Layton, P. Fifth-generation air warfare. *Aust. Def. Force J.* **2018**, *204*, 23–32.
3. Stillion, J. *Trends in Air-to-Air Combat: Implications for Future Air Superiority*; Center for Strategic and Budgetary Assessments: Washington, DC, USA, 2015.
4. Fan, H.; Zhang, P. The challenges for air-to-air missile. *Aero Weapon.* **2017**, *2*, 7.
5. Yi, Y.W. *Word Missiles Book*; Military Science Publishing House: Beijing, China, 2011.
6. Fan, H.; Cui, H.; Tian, G. A review on the 70-year development of air-to-air missiles. *Aero Weapon.* **2016**, *291*, 7–16.
7. Wasserbly, D. Adding SHORAD: US Army rebuilds its short-range air defences. *Jane's Int. Def. Rev.* **2018**, *51*, 41–45.
8. Ren, M.; Wen, L.; Li, S. Research on Foreign Air-to-Air Missiles' Development in 2018. *Aero Weapon.* **2019**, *26*, 1–9.
9. Felstead, P. Nammo Applies Its Ramjet Technology to Ground and Air-launched Missiles. *Jane's Def. Wkly.* **2019**, *56*, 8.
10. Liu, H.; Zhou, J.; Zhang, S. Launch dynamics of airborne missile with large maneuvering flight. *Syst. Eng. Electron.* **2018**, *40*, 2305–2310.
11. Ren, M.; Liu, Q.; Liu, J. Research on Foreign Air-to-Air Missiles' Development in 2019. *Aero Weapon.* **2020**, *27*, 17–24.
12. Zhang, R.; Zhang, L.; Sun, S.; Li, H. Development of Foreign Missile Techs and Equipment in 2020. *Aerosp. China* **2021**, *3*, 67–70.
13. Wu, Z.; Hong, X.; Li, D.; Zhao, L. *Air-to-Air Missile Radar Guidance Systems Design*; National Defense Industry Press: Beijing, China, 2007.
14. CSBA. *Advanced Medium Range Air-to-Air Missile*; FY 2019 Program Acquisition Costs by Weapon System; CSBA: Washington, DC, USA, 2018.
15. CSBA. *Operational Test and Evaluation*; FY 2017 Annual Report; CSBA: Washington, DC, USA, 2018.
16. Liao, S.; Wu, C.; Duan, J. Launch Dynamics Modeling and Analysis on Influencing Factors for Airborne Missile. *J. Proj. Rocket. Missiles Guid.* **2013**, *33*, 153–156.
17. Zhao, L.; Jiang, Y.; Wei, X.; Ma, L.; Li, X. Horizontal backward launch dynamics modeling and analysis. *Int. J. Aerosp. Eng.* **2019**, *2019*, 4098398. [CrossRef]
18. Liu, H.; Zhou, J.; Zhang, S. Launch Dynamics Characteristics Research of Air-to-Air Missile under Large Maneuvering Flight of Steal Aircraft. *J. Vib. Shock* **2018**, *37*, 24–29.
19. Xu, B.; Yang, J.; Liu, G.; Zhang, W. Modeling and Simulation of Eject Launcher for Airborne Missile. *J. Syst. Simul.* **2011**, *23*, 51–54.
20. Liao, Z.; Wang, Q. Influence and countermeasures of radar seeker pointing error on missile guidance. *Syst. Eng. Electron.* **2021**, *43*, 519–525.
21. Barton, D. Radar system analysis and modeling. *IEEE Aerosp. Electron. Syst. Mag.* **2005**, *20*, 23–25. [CrossRef]
22. Blake, L. Recent advancements in basic radar range calculation technique. *IRE Trans. Mil. Electron.* **1961**, *MIL-5*, 154–164. [CrossRef]
23. Bao, M.; Zhou, S.; Xing, M. Processing Missile-Borne SAR Data by Using Cartesian Factorized Back Projection Algorithm Integrated with Data-Driven Motion Compensation. *Remote Sens.* **2021**, *13*, 1462. [CrossRef]